
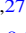










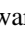

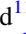

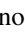


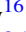
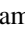


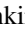


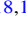







TESS Giants Transiting Giants. III. An Eccentric Warm Jupiter Supports a Period –Eccentricity Relation for Giant Planets Transiting Evolved Stars

Samuel K. Grunblatt^{1,2,26} , Nicholas Saunders^{3,27} , Ashley Chontos^{3,4,28} , Soichiro Hattori⁵ , Dimitri Veras^{6,7,8,29} , Daniel Huber³ , Ruth Angus^{1,2,5} , Malena Rice^{9,10,30} , Katelyn Breivik² , Sarah Blunt^{11,27} , Steven Giacalone^{12,27} , Jack Lubin¹³ , Howard Isaacson^{12,14} , Andrew W. Howard¹¹ , David R. Ciardi¹⁵ , Boris S. Safonov¹⁶ , Ivan A. Strakhov¹⁶ , David W. Latham¹⁷ , Allyson Bieryla¹⁷ , George R. Ricker⁹ , Jon M. Jenkins¹⁸ , Peter Tenenbaum^{18,19} , Avi Shporer⁹ , Edward H. Morgan⁹ , Veselin Kostov^{20,21} , Hugh P. Osborn^{9,22} , Diana Dragomir²³ , Sara Seager^{9,24,25} , Roland K. Vanderspek⁹ , and Joshua N. Winn⁴ 

¹American Museum of Natural History, 200 Central Park West, Manhattan, NY 10024, USA; sgrunblatt@amnh.org

²Center for Computational Astrophysics, Flatiron Institute, 162 5th Avenue, Manhattan, NY 10010, USA

³Institute for Astronomy, University of Hawai'i at Mānoa, 2680 Woodlawn Drive, Honolulu, HI 96822, USA

⁴Department of Astrophysical Sciences, Princeton University, 4 Ivy Lane, Princeton, NJ 08544, USA

⁵Department of Astronomy, Columbia University, 550 West 120th Street, New York, NY, USA

⁶Centre for Exoplanets and Habitability, University of Warwick, Coventry CV4 7AL, UK

⁷Centre for Space Domain Awareness, University of Warwick, Coventry CV4 7AL, UK

⁸Department of Physics, University of Warwick, Coventry CV4 7AL, UK

⁹Department of Physics and Kavli Institute for Astrophysics and Space Research, Massachusetts Institute of Technology, Cambridge, MA 02139, USA

¹⁰Department of Astronomy, Yale University, New Haven, CT 06511, USA

¹¹Cahill Center for Astronomy & Astrophysics, California Institute of Technology, Pasadena, CA 91125, USA

¹²Department of Astronomy, University of California Berkeley, Berkeley, CA 94720, USA

¹³Department of Physics & Astronomy, University of California Irvine, Irvine, CA 92697, USA

¹⁴Centre for Astrophysics, University of Southern Queensland, Toowoomba, QLD, Australia

¹⁵Caltech/IPAC-NASA Exoplanet Science Institute, Pasadena, CA 91125, USA

¹⁶Sternberg Astronomical Institute, M.V. Lomonosov Moscow State University, 13, Universitetskij pr., 119234, Moscow, Russia

¹⁷Center for Astrophysics | Harvard & Smithsonian, 60 Garden Street, Cambridge, MA 02138, USA

¹⁸NASA Ames Research Center, Moffett Field, CA 94035, USA

¹⁹SETI Institute, Mountain View, CA 94043, USA

²⁰NASA Goddard Space Flight Center, 8800 Greenbelt Road, Greenbelt, MD 20771, USA

²¹SETI Institute, 189 Bernardo Ave., Suite 200, Mountain View, CA 94043, USA

²²NCCR/Planet-S, Universität Bern, Gesellschaftsstrasse 6, 3012 Bern, Switzerland

²³Department of Physics and Astronomy, University of New Mexico, 210 Yale Boulevard NE, Albuquerque, NM 87106, USA

²⁴Department of Earth, Atmospheric, and Planetary Sciences, Massachusetts Institute of Technology, 77 Massachusetts Avenue, Cambridge, MA 02139, USA

²⁵Department of Aeronautics and Astronautics, Massachusetts Institute of Technology, 77 Massachusetts Avenue, Cambridge, MA 02139, USA

Received 2022 August 29; revised 2022 November 18; accepted 2022 November 25; published 2023 January 10

Abstract

The fate of planets around rapidly evolving stars is not well understood. Previous studies have suggested that, relative to the main-sequence population, planets transiting evolved stars ($P < 100$ days) tend to have more eccentric orbits. Here we present the discovery of TOI-4582 b, a $0.94^{+0.09}_{-0.12} R_J$, $0.53 \pm 0.05 M_J$ planet orbiting an intermediate-mass subgiant star every 31.034 days. We find that this planet is also on a significantly eccentric orbit ($e = 0.51 \pm 0.05$). We then compare the population of planets found transiting evolved ($\log g < 3.8$) stars to the population of planets transiting main-sequence stars. We find that the rate at which median orbital eccentricity grows with period is significantly higher for evolved star systems than for otherwise similar main-sequence systems. In general, we observe that mean planet eccentricity $\langle e \rangle = a + b \log_{10}(P)$ for the evolved population with significant orbital eccentricity where $a = -0.18 \pm 0.08$ and $b = 0.38 \pm 0.06$, significantly distinct from the main-sequence planetary system population. This trend is seen even after controlling for stellar mass and metallicity. These systems do not appear to represent a steady evolution pathway from eccentric, long-period planetary orbits to circular, short-period orbits, as orbital model comparisons suggest that inspiral timescales are uncorrelated with orbital separation or eccentricity. Characterization of additional evolved planetary systems will distinguish effects of stellar evolution from those of stellar mass and composition.

Unified Astronomy Thesaurus concepts: Exoplanets (498); Stellar evolution (1599); Star-planet interactions (2177); Transits (1711); Extrasolar gaseous giant planets (509)

²⁶ Kalbfleisch Fellow.

²⁷ NSF Graduate Research Fellow.

²⁸ Henry Norris Russell Fellow.

²⁹ STFC Ernest Rutherford Fellow.

³⁰ 51 Pegasi b Fellow.

1. Introduction

Though exoplanets have been known around evolved stars at orbital separations >1 au for decades (e.g., Hatzes et al. 2003), planets at smaller separations around evolved stars were expected to be engulfed owing to angular momentum exchange through tides (Hut 1981; Villaver & Livio 2009). In this paper, we consider a star to be evolved if its surface gravity g is less than one-fourth of the surface gravity of the Sun (i.e., $g \lesssim 6300 \text{ cm s}^{-2}$,

or $\log g < 3.8$). Until recently, though over 100 planets were known on orbits larger than 1 au around evolved stars as defined here, no planets were known on orbits smaller than 0.5 au around evolved stars (Schlaufman & Winn 2013; Villaver et al. 2014; Reffert et al. 2015).

The discovery of Kepler-91 b, a Jupiter-sized planet orbiting a $6.3 R_{\odot}$, $\log g < 3.0$ star every 6.25 days (Lillo-Box et al. 2014; Barclay et al. 2015), and subsequent discoveries with the NASA Kepler mission and its extension K2 (Borucki et al. 2010; Howell et al. 2014), have proven that planets can survive at short periods around evolved stars (Huber et al. 2013; Almenara et al. 2015; Van Eylen et al. 2016; Chontos et al. 2019). These short-period, Jupiter-sized planets have proven useful for studying planet inflation and star–planet interaction, revealing that planets can become inflated at late times (Grunblatt et al. 2016; Lopez & Fortney 2016; Grunblatt et al. 2017). Studies of planet occurrence have revealed that these planets are more common than predictions suggested (e.g., Schlaufman & Winn 2013), with hot Jupiters being found to be similarly common around main-sequence and evolved stars (Grunblatt et al. 2019).

In addition, planets transiting evolved stars have been found to reside on more eccentric orbits, on average (Grunblatt et al. 2018; Jones et al. 2018). Stellar evolution is predicted to enhance the population of closer-in ($\lesssim 0.1$ au) planets on moderately eccentric orbits, as stellar tides begin to dominate orbital dynamics at larger and larger separations and cause planetary inspiral and orbit circularization simultaneously, producing a transient population of moderately eccentric planets on short periods around evolved stars (Villaver et al. 2014). However, this cannot explain why these planets had larger (>0.1 au), highly eccentric orbits during the main sequence.

These large main-sequence eccentricities can be potentially explained by planet–planet scattering events in the initial stages of planetary system formation and evolution. Stars with higher masses or higher metallicities might have formed in conditions that led to multiple closely spaced giant planets, which in turn could have led to planet–planet scattering events, known to excite orbit eccentricities (Freikh et al. 2019). In addition, evolved transiting planetary system host stars are more massive and metal-rich than the Sun, on average (Grunblatt et al. 2019).

Unfortunately, the majority of evolved transiting planetary systems currently known cannot constrain the rate of planet–planet scattering events in these systems owing to the possibility of strong tidal dissipation during hot Jupiter formation, which effectively erases the evidence for the formation pathways of hot Jupiter systems (Dawson & Johnson 2018). In contrast, planets at larger orbital separations (>0.1 au) do not experience such strong tidal dissipation and thus may effectively “fossilize” evidence for planet–planet scattering by maintaining high eccentricities at late evolutionary stages. If planets on longer periods around evolved stars tend to be more eccentric than planets around main-sequence stars, this can be interpreted as evidence for higher rates of planet–planet scattering in these systems. Determining whether planet–planet scattering is more prevalent in evolved planetary systems than in equivalent main-sequence systems indicates whether this scattering is a result of post-main-sequence system evolution or initial planetary system formation, essential to understanding the long-term stability of planetary systems.

At least one planet has been found transiting an evolved host star with a period longer than 50 days, Kepler-432 b (Ciceri et al. 2015; Quinn et al. 2015). This planet has a particularly high orbital eccentricity ($e = 0.54 \pm 0.03$). This high eccentricity, as well as evidence for the existence of an additional companion in the system, suggests that Kepler-432 is potentially a dynamically active planetary system. It is unclear what role each of the components of the system has played in producing the currently observed orbital configuration, but planet–planet interactions likely played an important role in sculpting the system architecture.

Radial velocity (RV) studies have also revealed a long-period planet population around evolved stars at separations >0.5 au. These planets have a wide range in eccentricities but interestingly appear to have generally lower eccentricities than planets of similar mass and orbital separation around main-sequence stars (Jones et al. 2014; Grunblatt et al. 2018). This is seemingly at odds with the moderately high eccentricities of planets observed at smaller periods around evolved stars but may imply that planet–planet scattering is common within 0.5 au of evolved host stars and rarer at larger orbital separations. As gas giant planets are believed to form beyond 1 au, this suggests that most transiting planets observed around evolved stars have undergone some sort of planet–planet scattering, while planets detected at larger separations have not experienced as much dynamical interaction. The characterization of more planets around evolved systems with intermediate orbital periods (0.1–1 au) will reveal whether this difference in eccentricity distribution is more dependent on orbital separation or is a selection effect, and whether a turnover in median eccentricity can be found at longer periods. A search for transiting planets across the entire sky will be essential for detection of these intermediate orbital period planets around evolved stars.

The Transiting Exoplanet Survey Satellite (TESS; Ricker et al. 2014) is enabling the discovery of a predicted $\sim 14,000$ planets (Sullivan et al. 2015; Barclay et al. 2018; Kunimoto et al. 2022) across the entire sky. During its 2 yr primary mission (2018 July–2020 July), the space telescope observed stars in full-frame images (FFIs) with a 30-minute observing cadence and completed 1 yr of observations in each of the northern and southern ecliptic hemispheres. Each year was split into 13 observing sectors that stretched from the ecliptic pole toward the ecliptic plane, moving every ~ 27 days. Targets near the ecliptic pole were observed in multiple sectors, in some cases providing a full year of photometry, while targets closer to the ecliptic plane were observed in fewer sectors. According to the NASA Exoplanet Science Institute (NExSci) archive,³¹ TESS has already led to the discovery of 100+ confirmed planets and 5000+ project candidates (Guerrero et al. 2021). Of the planets confirmed to date, only a handful orbit post-main-sequence stars, most of which have only just begun evolution off of the main sequence (e.g., Huber et al. 2019; Nielsen et al. 2019; Wang et al. 2019; Eisner et al. 2020; Rodriguez et al. 2021; Grunblatt et al. 2022; Khandelwal et al. 2022; Montalto et al. 2022; Saunders et al. 2022; Wittenmyer et al. 2022).

Here we present analysis of the TESS prime mission and available spectroscopic and imaging data for TOI-4582 and place this planetary system into context of the known population of giant planets transiting evolved stars. We find

³¹ nexsci.caltech.edu

that TOI-4582 b seems to support the existence of a period–eccentricity correlation for planets transiting evolved stars and that the population of transiting planets around evolved stars is significantly distinct from the population of similar planets transiting main-sequence stars in the period–eccentricity plane. We investigate whether this difference could have arisen from other fundamental differences between these populations, such as their stellar masses and metallicities, or whether it is more clearly correlated with evolution proxies such as stellar radius or age. We also show how the period–eccentricity relation is relatively insensitive to our definition of “evolved,” and we investigate whether this correlation arises from a clear evolutionary pathway from longer-period, eccentric orbits to small, circular orbits at late evolutionary stages. Finally, we consider future prospects for investigating the evolution of planetary architectures.

2. Observations

2.1. TESS Photometry

TOI-4582 b was discovered as part of our survey to identify and confirm planets around evolved stars using TESS FFIs (Guest Investigator programs GO22102, GO3151, GO4179). TOI-4582 was observed by the TESS prime mission in Sectors 14–26, from 2019 July 18 to 2020 July 4. Using the TESS Input Catalog (TICv8; Stassun et al. 2019), we made cuts based on Gaia color ($B_p - R_p > 0.9$ mag), absolute magnitude ($M_G < 4.0$ mag), and apparent magnitude ($m_T < 13$ mag) in order to limit our sample to relatively bright, evolved stars. We developed the `giants`³² Python package for accessing, detrending, and searching TESS observations for periodic transit signals (Saunders et al. 2022). The details of how this pipeline processes TESS FFI data are described in Saunders et al. (2022), but in short, the `giants` pipeline uses a principal component analysis approach to detrending. In summary, a light curve is produced by creating an 11×11 pixel cutout for all sectors in which the target is observed by TESS and then drawing an aperture on the cutout around the target based on a threshold flux. Ten principal components common to the cutout outside the chosen aperture are then identified and subtracted from the flux within the aperture, leaving the signal that is present within the aperture without significant background contribution. We also present the `giants` light curves along with the “SAP FLUX” and “KSPSAP FLUX” light curves produced by the MIT Quick Look Pipeline (Huang et al. 2020) in Figure 1, which use a background subtraction and contamination factor-based approach to produce light curves, where the “KSPSAP FLUX” light curve also includes a spline-based detrending step. TOI-4582 b is on a long-period, highly eccentric orbit, which was not detected by other early TESS transit searches owing to its long transit duration.

However, a later transiting planet search by the TESS Science Processing Operations Center (SPOC; Jenkins et al. 2016) of sectors 40 and 41 on 2021 September 14 detected the signatures of two transits of TOI-4582 b (Jenkins 2002; Jenkins et al. 2010, 2020), which was fitted with an initial limb-darkened transit model (Li et al. 2019) and passed all the diagnostic tests (Twicken et al. 2018). The TESS Science Office issued an alert for TOI-4582 b on 2021 November 11 reviewing the data validation reports (Guerrero et al. 2021). A

subsequent search by the SPOC of sectors 40, 41, and 46–50 redetected the transit signatures and yielded difference image centroiding results that located the source of the transits to within $1''.8 \pm 2''.9$ from the host star.

We used our `giants` pipeline to produce TESS light curves for all stars that passed our aforementioned cuts. We produced approximately 540,000 light curves from the first 2 yr of data from the TESS mission. We then performed an automated box least squares (BLS) search on these targets and produced summary plots using the BLS output, as well as TIC information and the pixel cutout. These summary plots were then visually inspected, during which TOI-4582 was flagged for potential rapid ground-based follow-up. The results of this visual inspection will be verified by computational techniques, and a subsequent catalog of planet candidates transiting evolved stars will be released in the near future (N. Saunders et al. 2022, in preparation). Eleven sectors of data were available for TOI-4582 b at the conclusion of the TESS prime mission, during which nine transits were observed. Additional data are currently being taken for this target as part of the TESS extended mission.

We illustrate the phase-folded light curves of TOI-4582 in Figure 2. The planet transit can be seen at a phase of 6 days in the “SAP FLUX” and `giants` light curves. The transit duration has been measured to be 11.952 ± 1.368 hr. As the “KSPSAP FLUX” pipeline is smoothed using a spline approach with a window length of 0.3 days, it is likely that the transit of TOI-4582 b was smoothed to the point where it is no longer visible. This hypothesis is supported by the lack of transit seen in the phase-folded “KSPSAP FLUX” light curve, while transits are clearly seen in the “SAP FLUX” and `giants` light curves. The principal component analysis approach to detrending used by the `giants` pipeline removes trends that are seen in neighboring TESS pixels, thus reducing the effect of scattered light and TESS orbital properties while preserving the transit signal, which is detected only in the target pixels. This approach can fail in sectors where background light is sufficiently strong both inside and outside the chosen aperture for the target, here resulting in the data gap around BJD 2,458,850 seen in the `giants` light curve in Figure 1.

In addition, a significant difference in transit depth is measured between the “SAP FLUX” and `giants` light curves, where the “SAP FLUX” transit is $\approx 15\%$ deeper than the `giants` transit, implying a planet radius that is $\approx 8\%$ larger. This difference and its implications are discussed further in Section 4.

2.2. Radial Velocity Measurements

RV observations were taken with the HIRES spectrograph on the Keck I telescope on Maunakea, Hawaii (Vogt et al. 1994). HIRES has a resolving power of $R \approx 60,000$ and wavelength coverage between ~ 350 and ~ 620 nm. Twelve RV measurements were taken of TOI-4582 between 2021 May 27 and October 17. We list our RV measurements and uncertainties in Table 1.

In addition, two RV observations were taken between 2021 November and 2022 March using the TRES spectrograph on the 1.5 m FLWO telescope (Fűrész et al. 2008). These measurements revealed an RV offset of 99 m s^{-1} that is in phase with the photometric ephemeris and is consistent with a planetary-mass companion. Given the higher precision and phase coverage of Keck/HIRES, we only list the Keck/HIRES RV measurements here.

³² <https://github.com/nksaunders/giants>

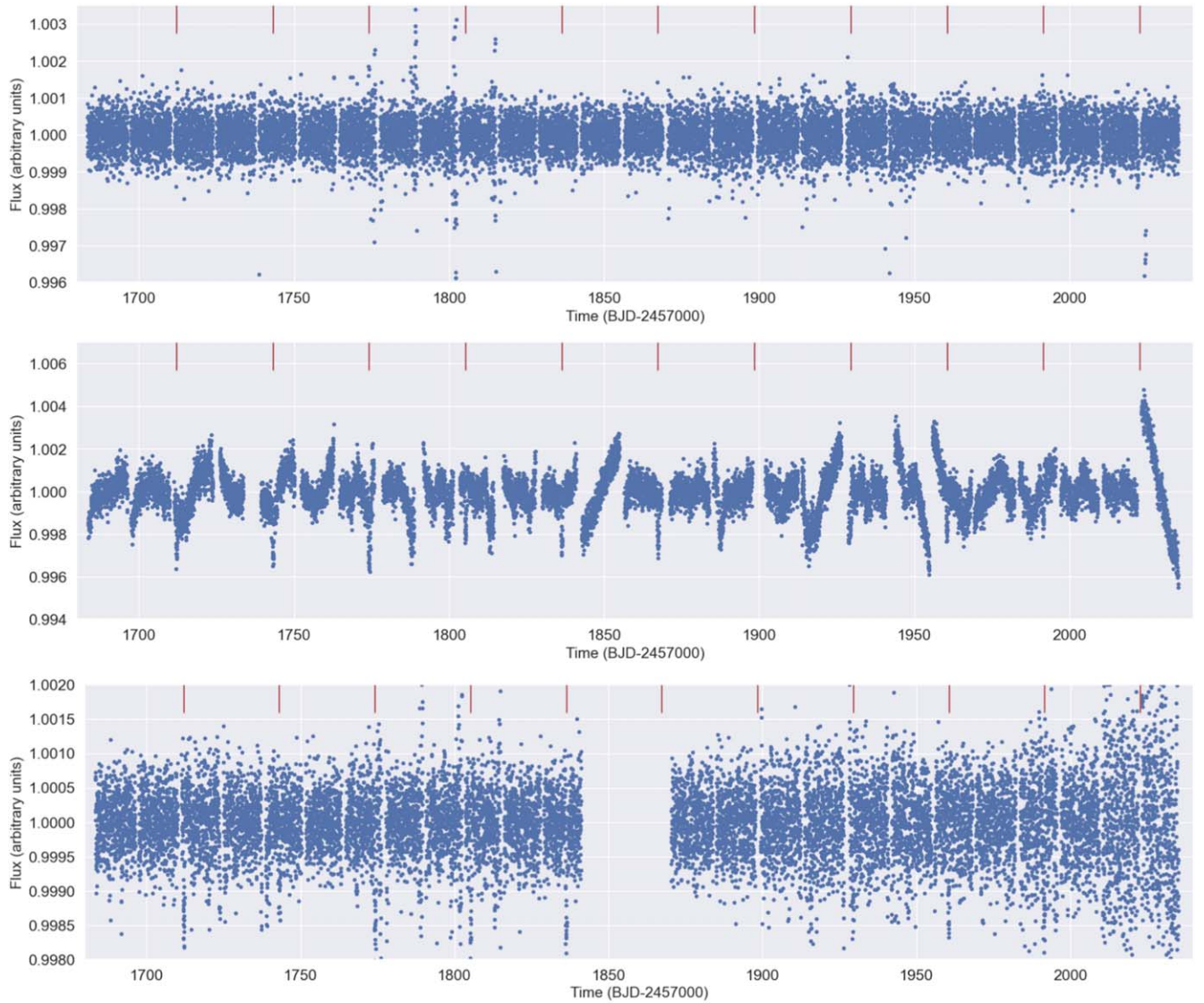


Figure 1. Unfolded, full TESS prime mission light curves of TOI-4582 with “KSPSAP FLUX,” “SAP FLUX,” and `giants` flux values (from top to bottom). Transits are indicated by red fiducial marks. While the “KSPSAP FLUX” smoothing removes both transits and long-term trends visible in the “SAP FLUX” light curve, the `giants` approach to detrending of the light curve removes long-term variability while preserving planet transits, despite their long duration. However, one sector of data around BJD 2,458,850 is not included in the `giants` light curve owing to poor background subtraction.

3. Host Star Characterization

3.1. High-resolution Spectroscopy

We used `SpecMatch-Syn` to measure the metallicity, surface gravity, and effective temperature of the host star TOI-4582 from our HIRES spectra (Petigura 2015). We then used `isoclassify` (Huber et al. 2017) to combine Gaia parallax measurements with spectroscopic information to determine stellar properties, listed in Table 2. We find that these results are in good agreement with an independent analysis of stellar parameters using the stellar parameter classification (SPC) technique (Buchhave et al. 2012), which follows a similar general procedure to `isoclassify` but uses different stellar models to describe spectral observations of this target with the TRES spectrograph (Fűrész et al. 2008). SPC and `SpecMatch-Syn` both cross-correlate an observed spectrum against a grid of synthetic spectra and use the correlation peak heights to fit a three-dimensional surface in order to find the best combination of atmospheric parameters.

In this case, the SPC analysis did not use priors to constrain stellar parameters based on a grid of isochrones, as the overlap of isochrone grids of different metallicities on the subgiant branch used by SPC can result in biased determinations of stellar surface gravities. As the subgiant stage of evolution is relatively short, fitting to isochrone grids can provide very precise parameter constraints for subgiant stars. However, fine-tuning of stellar model parameters that are poorly constrained such as mixing length can result in substantial changes in the inferred intrinsic stellar parameters of stars on the subgiant branch. Thus, we report errors that are modestly larger than what is returned from our isochrone-based analysis to more accurately reflect realistic uncertainties on the intrinsic stellar parameters, inflating errors to match the known fractional systematic uncertainty floor for stars at this evolutionary state (Tayar et al. 2022).

Figure 3 shows an H-R diagram with evolutionary tracks downloaded from the MESA Isochrones & Stellar Tracks (MIST; Dotter 2016; Choi et al. 2016; Paxton et al. 2011). We

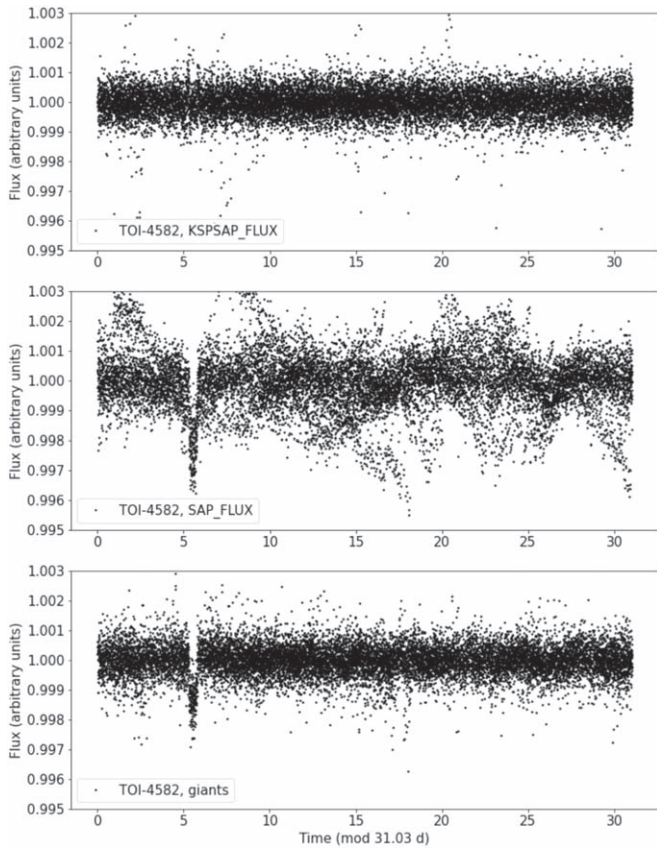


Figure 2. Phase-folded light curves of TOI-4582 using the QLP “KSPSAP FLUX,” “SAP FLUX,” and giants fluxes (from top to bottom). Clear differences in transit depth and shape and light-curve scatter can be seen between the different light curves.

Table 1
Radial Velocities and Uncertainties Measured for TOI-4582 from Keck/HIRES

Time (JD)	Relative RV (m s^{-1})
2,459,361.983	30.9 ± 0.8
2,459,376.920	-24.3 ± 1.0
2,459,385.849	-11.7 ± 1.6
2,459,399.906	-3.5 ± 1.4
2,459,406.904	-11.9 ± 1.0
2,459,435.825	-21.6 ± 1.4
2,459,441.914	-17.1 ± 1.4
2,459,451.859	26.0 ± 1.5
2,459,456.838	21.6 ± 1.5
2,459,475.790	-7.6 ± 1.7
2,459,484.773	44.7 ± 1.6
2,459,504.787	-25.0 ± 1.9

Note. The RVs have been sorted in time.

have shown the positions of all host stars of confirmed planets found by our TESS Giants Transiting Giants Guest Investigator program. As all five host stars have roughly the same mass and metallicity ($M_* \approx 1.5 M_\odot$, $[\text{Fe}/\text{H}] \approx 0.25$ dex), we suggest that these systems may represent an evolutionary sequence for post-main-sequence, intermediate-mass stars. We find that TOI-4582 lies at a late subgiant stage of evolution between the evolutionary stage of subgiants TOI-2184 and TOI-4329 and giant stars TOI-2337 and TOI-2669.

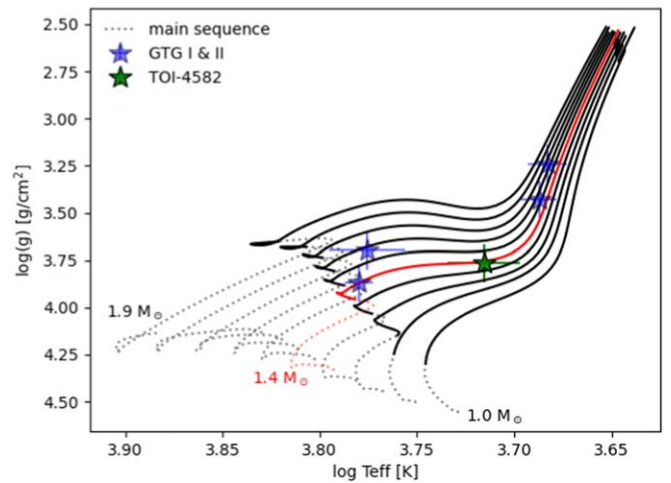


Figure 3. Position of TOI-4582 along with the other planet hosts from the Giants Transiting Giants program shown on an H-R diagram. All host stars have evolved off of the main sequence onto the subgiant and red giant branch. We also illustrate MIST evolutionary tracks of 1–2 M_\odot , +0.25 $[\text{Fe}/\text{H}]$ dex stars in 0.1 M_\odot increments for reference. We have highlighted a MIST evolutionary track for a 1.4 M_\odot , $[\text{Fe}/\text{H}] = 0.25$ dex star in red, illustrating the evolutionary sequence directly probed here.

Table 2
Effective Temperature, Surface Gravity, and Metallicity Were Determined Using SpecMatch-Syn Fits to Keck/HIRES Spectra

<i>Target IDs</i>	
TOI	4582
TIC	219854519
TYC	4421-01472-1
2MASS	J17072649+6851562
Gaia DR2	1636984973365053056
<i>Coordinates</i>	
RA(J2015.5)	17:07:26.43
Dec(J2015.5)	+68:51:56.25
<i>Characteristics</i>	
TESS mag	10.54
Radius R_*	$2.5 \pm 0.1 R_\odot$
Mass M_*	$1.34 \pm 0.06 M_\odot$
T_{eff}	5190 ± 100 K
$\log(g)$	3.77 ± 0.04 dex
$[\text{Fe}/\text{H}]$	0.17 ± 0.06 dex
$v \sin i$	2.7 ± 1.0 km s^{-1}
Age	4 ± 1 Gyr
Density ρ_*	$0.084 \pm 0.005 \rho_\odot$

Note. Stellar mass, radius, age, and density are derived from an isoclassify fit to HIRES spectroscopic observations, Gaia parallaxes, and 2MASS K -band photometry. We inflate our error bars reported from isochrones to reflect more realistic uncertainties following the reasoning of Tayar et al. (2022).

3.2. Rotation of TOI-4582

Outside of the transit, the “SAP FLUX” light curve of TOI-4582 shows smooth, longer-period variability that may be associated with the rotation of the host star. Measurement of the stellar rotation period can constrain the strength of magnetic activity and tidal interaction with the orbiting planet. Furthermore, although stellar rotation periods cannot yet be used to constrain the age of subgiant stars, as stellar rotation rates have been directly measured for only a handful of subgiants, a measurement of the stellar rotation rate in this

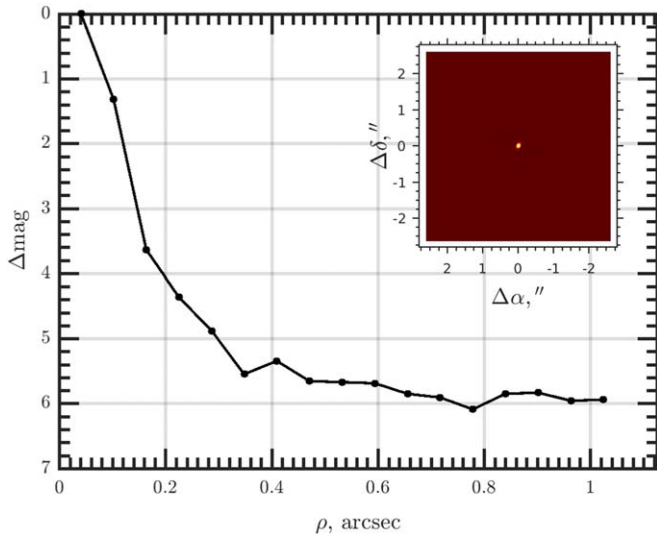


Figure 4. Contrast curve for TOI-4582 based on speckle polarimeter imaging taken with the Sternberg Astronomical Institute 2.5 m telescope, with the corresponding speckle autocorrelation function shown in the inset. TOI-4582 appears to be a single star based on imaging data from multiple sources and astrometric information from Gaia.

system may provide information about the correlation between age and rotation rates of subgiants in the future and thus is worth reporting if it can be measured using reliable methods. In order to produce a light curve particularly sensitive to rotational variation, we use the `unpopular` package to perform causal pixel modeling and isolate the long-period variability of this target (Hattori et al. 2022). We find a tentative rotation period detected at $P \sim 73$ days, with different choices of detrending parameters resulting in rotation periods detected between 71 and 77 days, in agreement with rotation rates and signal amplitudes reported by Santos et al. (2021) for similar subgiant targets. Confirmation of this signal with other high-cadence photometric surveys, such as the Zwicky Transient Facility (Bellm et al. 2019), will test the validity and accuracy of this stellar rotation period measured here.

3.3. Constraints on Binarity of TOI-4582

TOI-4582 was observed with the Speckle Polarimeter (SPP; Safonov et al. 2017) on the 2.5 m telescope at the Caucasian Observatory of the Sternberg Astronomical Institute on 2022 March 14 using the Ic-band filter near $0.9 \mu\text{m}$. SPP uses an Electron Multiplying CCD Andor iXon 897 as a detector. The atmospheric dispersion compensator was employed. The detector has a pixel scale of $20.6 \text{ mas pixel}^{-1}$, and the angular resolution of the observations is 89 mas, with a field of view of $5'' \times 5''$ centered on TOI-4582. The power spectrum was estimated from 4000 frames with 30 ms exposure. The contrast curve for the SAI observations can be seen in Figure 4, which shows the detection limits in contrast (Δm) versus angular separation from the point-spread function center in arcseconds for the filter wavelength. The inset image is the speckle autocorrelation function for the observation. We did not detect any stellar companions brighter than $\Delta m = 4''0$ and $5''6$ at $0''2$ and $0''5$, respectively. TOI-4582 was also observed by the NESSI instrument on the 3.5 m WIYN telescope at the Kitt Peak Observatory in Arizona (Scott et al. 2018). Observations were taken on 2022 April 21 using the 832 nm filter. No additional stars can be identified within $4''$ of our target in

either imaging data set. The difference image centroiding results produced by SPOC also agree with the results of the high-resolution imaging.

Furthermore, the Gaia astrometric noise metric RUWE for TOI-4582 is low (0.77), indicative that the star is not in a wide binary system that could be resolved by Gaia astrometry (typical RUWE values for binaries are >1.4). Additionally, no evidence of a spectroscopic binary can be seen in the spectra of this star, placing limits on a companion of similar brightness for this star. Specifically, we use the Kolbl et al. (2015) routine to determine limits on spectroscopic binarity and find no evidence for a spectroscopic companion brighter than 1% of the brightness of the primary with an RV shift of 10 km s^{-1} or larger from the primary. The RV measurements of these systems do not show any significant linear or quadratic trends with time, suggesting that this star is single and not part of a binary system.

4. Planet Characterization

4.1. Model Fit

We used the `exoplanet` Python package to simultaneously fit a model to the photometry and RV observations (Foreman-Mackey et al. 2020). The data input to our model included all Keck/HIRES RV observations and all sectors of TESS FFI photometry available from the first 3 yr of the TESS mission. Our model used the stellar parameters given in Table 2.

Our initial choices of planet period and depth were taken from the BLS-search-determined values produced during the transit search described in Section 2.1. For limb darkening, we use the quadratic model prescribed by Kipping (2013) to provide a two-parameter model with uninformative sampling. We parameterized eccentricity using the single-planet eccentricity distribution of Van Eylen et al. (2019). We present our best-fit models to the giants light curve and RV data for TOI-4582 in Figure 5 and Table 3.

We also performed a joint RV and transit fit using the “SAP FLUX” light curve (in addition to the giants light curve). We find a planet radius of $0.88 \pm 0.06 R_J$ using the giants light curve and $1.01 \pm 0.03 R_J$ using the “SAP FLUX” light curve. The range in planet radii determined by these fits is $0.13 R_J$, significantly larger than the uncertainty in planet transit depth estimated from any fit to the available data. We note that this discrepancy in transit depth between the giants pipeline and other pipelines has been seen in other transiting planet examples (such as TOI-4329; Grunblatt et al. 2022) and may be related to background light contamination or baseline flux determination within the multipixel aperture, which the giants pipeline does not account for in the same fashion as the “SAP FLUX” or “KSPSAP FLUX” pipelines. We note that an independent analysis of the short-cadence SPOC light curve produced by the TESS extended mission of this target successfully detects this transit and measures an $R_p/R_* = 0.0352$ for this system, almost identical to the value reported by our giants pipeline analysis. Despite this, we choose to keep our error estimates conservative, and thus we adopt the full range of radius uncertainties from both light curves as our final reported uncertainties and the mean transit radius between the giants and “SAP FLUX” light-curve fits, and we report a planet radius of $0.94^{+0.09}_{-0.12} R_J$ for TOI-4582 b. Future observations with facilities with better resolution capable of using smaller photometric apertures, such as those used by the

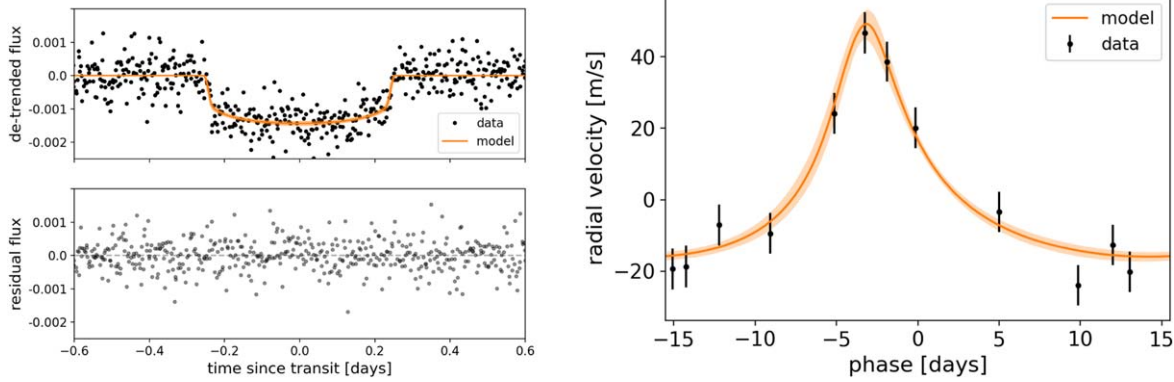


Figure 5. Left: the light curve of TOI-4582 folded at a period of 31.034 ± 0.001 days. The detrended photometry is shown in black, with the transit model from `exoplanet` overplotted in orange. The residuals to the model are shown in the bottom panel. Right: all Keck/HIRES RV observations of TOI-4582 b, along with the best-fit `exoplanet` model used in this analysis, where the time axis has been folded at the orbital period of the planet. RV errors include contributions from both measurement and a white-noise term within the model.

Las Cumbres Observatory Global Telescope array (Brown et al. 2013), will be able to confirm the true transit depth of this system, more precisely constraining the radius of TOI-4582 b. Despite the discrepancy in radius measurements using different TESS FFI light curves, our main conclusions about the system and its context in the larger known planet population are unaffected and would remain valid if the planet radius measured exclusively from either the “SAP FLUX” or giants light curve were used for this study.

5. Eccentricity Analysis

5.1. Eccentricity of TOI-4582 b

Both the planet transit and radial velocities measured in TOI-4582 show strong evidence for an eccentric planetary orbit. Using `exoplanet` to fit eccentricity using the single-planet system prior defined in Van Eylen et al. (2019), we measure an orbital eccentricity of $e = 0.51 \pm 0.05$ for TOI-4582 b. We note that the determined eccentricity is not sensitive to this choice of prior; the median eccentricity and uncertainties determined strongly agree with the presented values if a uniform prior between 0 and 1 is used instead. The eccentricity of $e = 0.51 \pm 0.05$ is among the most eccentric orbits ever found for a planet transiting an evolved star, as well as one of the longest orbital periods found for a planet transiting an evolved star. Only one other known transiting planet around an evolved star, Kepler-432, has a longer orbital period, and it interestingly displays a comparable orbital eccentricity (Ciceri et al. 2015; Quinn et al. 2015). Placing these systems in context of the known planets transiting evolved stars suggests that evolved stars may display a correlation between period and eccentricity that does not exist, or at least is not seen as clearly in main-sequence systems.

This may partially be due to the difficulty in detection of long-period ($\gtrsim 10$ days) planets with TESS, as well as the enhanced transit probability of planets on eccentric orbits relative to planets on circular orbits with the same period (Nelson & Davis 1972; Barnes 2007; Beatty & Seager 2010; Barclay et al. 2018).

However, the boost in transit probability due to eccentricity is relatively modest for all of the planets transiting evolved stars in our sample (a factor of 1.1 at an $e = 0.3$, or 1.33 at $e = 0.5$). Looking at orbital periods between 10 and 100 days,

two-thirds of the population of planets in our sample have eccentricities larger than 0.2, while only one-third of planets in similar systems transiting similar main-sequence stars do. An increase in transit probability of 1.3, larger than the true enhancement for this eccentric evolved population, to all the evolved systems observed is still insufficient to explain this overabundance of eccentric planets. We suggest that this may imply a different eccentricity distribution for planets transiting evolved stars than those transiting main-sequence stars, and we attempt to test this hypothesis below.

5.2. Eccentricity of the Evolved Planet Population: Distinction from Main-sequence Systems

The analysis of orbital eccentricities of exoplanet systems is essential to understanding planetary system formation and evolution (e.g., Chatterjee et al. 2008; Dawson & Johnson 2018). Earlier studies have shown evidence for dichotomies in the distribution of planet eccentricities between transiting and nontransiting planet populations, between single-planet and multiplanet systems, and between main-sequence and evolved systems (Xie et al. 2016; Grunblatt et al. 2018; Van Eylen et al. 2019). This may be driven by stellar evolution, which is known to directly sculpt the planet population through tidal effects, particularly at short periods (Hut 1981; Villaver et al. 2014; Hamer & Schlaufman 2019; Yee et al. 2020).

However, the effect of stellar evolution on planetary dynamics at longer periods is more unclear, due largely to the small population of known evolved transiting planetary systems. Evolved planet host stars tend to be more massive and metal-rich than most currently known main-sequence planet hosts. Enhancement in mass and metallicity might be associated with scattering events during system formation, which can result in a wider range of eccentricities for longer-period planets immediately after initial planet formation (Dawson & Murray-Clay 2013; Freikh et al. 2019). In addition, other dynamical interactions between planets such as secular angular momentum exchanges and Kozai-Lidov interactions can also excite planet eccentricities after initial formation and potentially produce hot Jupiters through high-eccentricity migration (Petrovich 2015a, 2015b; Naoz 2016). This process may produce more eccentric, long-period planets during main-sequence evolution, resulting in more eccentric planets and hot Jupiters in older systems. Thus, identifying

Table 3
Fit and Derived Parameters for TOI-4582 b

Parameter	Prior	Value
<i>Transit Fit Parameters</i>		
Orbital period P_{orb} (days)	$\log \mathcal{N}[31.06, 0.0015]$	days
Planet-to-star radius ratio R_p/R_*	$\mathcal{U}[0, 1]$	0.0351 ± 0.002
Transit epoch t_0 (BJD $-2,457,000$, TDB)	$\mathcal{N}[1712.0, 1.0]$	1712.177 ± 0.004
Impact parameter b	$P_\beta(e \in [0, 1])^a$	0.52 ± 0.08
Eccentricity e	single-planet dist. from Van Eylen et al. (2019)	0.51 ± 0.05
Argument of periastron Ω	$\mathcal{U}[-\pi, \pi]$	-0.166 ± 0.102
Limb-darkening coefficient q_1	$[0, 2]^b$	0.383 ± 0.224
Limb-darkening coefficient q_2	$[-1, 1]^b$	0.176 ± 0.327
<i>Radial Velocity Fit Parameter</i>		
Semi-amplitude K (m s^{-1})	$\mathcal{U}[0, 500]$	31 ± 3
<i>Derived Physical Parameters</i>		
Planet radius R_p (R_J)	$\mathcal{U}[0, 3]$	$0.94^{+0.09}_{-0.12}$
Planet mass M_p (M_J)	$\mathcal{U}[0, 300]$	0.53 ± 0.05

Notes.

^a This parameterization is described by the Beta distribution in Kipping et al. (2013).

^b Distributions follow the correlated two-parameter quadratic limb-darkening law from Kipping (2013).

Table 4
Known Giant Planets Transiting Evolved Stars with Significant Orbital Eccentricities

Name	Planet Mass (M_J)	Planet Radius (R_J)	Orbital Period (days)	Eccentricity	Stellar Mass (M_\odot)	Stellar Radius (R_\odot)	Metallicity	Source
HD 1397 b	0.41 ± 0.02	1.03 ± 0.03	11.535 ± 0.001	0.25 ± 0.03	1.32 ± 0.04	2.34 ± 0.05	0.29 ± 0.09	1
HD 221416 b	0.19 ± 0.02	0.84 ± 0.03	14.267 ± 0.004	0.115 ± 0.03	1.21 ± 0.07	2.94 ± 0.06	-0.08 ± 0.08	2
Kepler-91 b	0.76 ± 0.13	1.30 ± 0.07	6.246669 ± 0.00008	$0.018^{+0.040}_{-0.016}$	1.31 ± 0.10	6.30 ± 0.16	0.11 ± 0.07	3
Kepler-432 b	5.41 ± 0.32	1.15 ± 0.04	52.5011 ± 0.0001	0.51 ± 0.03	1.35 ± 0.10	4.16 ± 0.12	-0.07 ± 0.10	4
Kepler-435 b	0.84 ± 0.15	1.99 ± 0.18	8.600153 ± 0.000002	0.11 ± 0.07	1.54 ± 0.09	3.21 ± 0.30	-0.18 ± 0.11	5
Kepler-643 b	1.01 ± 0.20	0.91 ± 0.03	16.33889 ± 0.00001	0.37 ± 0.06	1.00 ± 0.07	2.52 ± 0.07	0.16 ± 0.10	6
Kepler-1658 b	5.88 ± 0.48	1.07 ± 0.05	3.84937 ± 0.00001	0.0628 ± 0.018	1.05 ± 0.15	3.91 ± 0.26	-0.18 ± 0.10	7
K2-39 b	0.125 ± 0.014	0.51 ± 0.06	4.60543 ± 0.0005	0.15 ± 0.08	1.19 ± 0.08	2.93 ± 0.21	0.32 ± 0.04	8
K2-97 b	0.48 ± 0.07	1.3 ± 0.1	8.4061 ± 0.0015	0.22 ± 0.08	1.16 ± 0.12	4.20 ± 0.14	0.42 ± 0.08	6
K2-99 b	0.97 ± 0.09	1.29 ± 0.05	18.249 ± 0.001	0.19 ± 0.04	$1.60^{+0.14}_{-0.10}$	3.1 ± 0.1	0.20 ± 0.05	9
K2-132 b	0.49 ± 0.06	1.3 ± 0.1	9.1751 ± 0.0015	0.36 ± 0.06	1.08 ± 0.08	3.85 ± 0.13	-0.01 ± 0.08	6
NGTS-20 b	2.98 ± 0.16	1.07 ± 0.04	54.18915 ± 0.00015	0.432 ± 0.023	1.47 ± 0.09	1.78 ± 0.05	0.15 ± 0.08	10
TOI-2184 b	0.65 ± 0.16	1.02 ± 0.05	6.90683 ± 0.00009	0.08 ± 0.07	1.53 ± 0.12	2.90 ± 0.14	0.14 ± 0.08	11
TOI-2337 b	1.60 ± 0.15	0.9 ± 0.1	2.99432 ± 0.00008	0.019 ± 0.017	1.33 ± 0.12	3.22 ± 0.06	0.39 ± 0.06	12
TOI-2669 b	0.61 ± 0.19	1.76 ± 0.16	6.2034 ± 0.0001	0.09 ± 0.05	1.19 ± 0.16	4.10 ± 0.04	0.10 ± 0.06	12
TOI-4582 b	0.53 ± 0.05	$0.94^{+0.09}_{-0.12}$	31.034 ± 0.001	0.51 ± 0.05	1.34 ± 0.02	2.51 ± 0.04	0.21 ± 0.06	13

References. (1) Nielsen et al. 2019; (2) Huber et al. 2019; (3) Barclay et al. 2015; (4) Quinn et al. 2015; (5) Almenara et al. 2015; (6) Grunblatt et al. 2018; (7) Chontos et al. 2019; (8) Van Eylen et al. 2016; (9) Smith et al. 2017; (10) Ulmer-Moll et al. 2022; (11) Saunders et al. 2022; (12) Grunblatt et al. 2022; (13) this work.

whether the similarities between the main-sequence single-planet transiting systems and evolved systems result from differences in intrinsic stellar properties, ages, and detection biases, or if the underlying planet populations of main-sequence and evolved stars are significantly different, will reveal the more general role of stellar evolution in sculpting planetary architectures.

Here we attempt to determine whether these populations are statistically distinct by comparing the transiting planet populations of evolved and main-sequence stars, introducing cuts to account for detection biases of planets that transit evolved stars, as well as intrinsic stellar property differences between these two planet populations, and then testing whether the dichotomy remains.

We compare the population of planets orbiting evolved (i.e., $\log g \leq 3.8$) stars as listed in Table 4 to the known population

of planets ($R_p \geq 0.4 R_J$) orbiting similar main-sequence stars ($M_* \geq 1.05 M_\odot$, $[\text{Fe}/\text{H}] > -0.2$ dex) in Figure 6. We consider all systems meeting the aforementioned stellar mass and metallicity cuts and with planet orbital eccentricities that were significantly nonzero (i.e., their orbital eccentricity was inconsistent with 0 within the listed, published uncertainties). We show the populations as contours determined from kernel density estimation in the top panel, as well as the individual planets in each population, where planets transiting evolved stars are shown in red and the larger, overall planet population is shown in gray. We also illustrate the approximate limit for eccentricity growth from planet-planet scattering events as a dashed black line.

These scattering events can be described as the transfer of the difference in angular velocity of two planets in the same

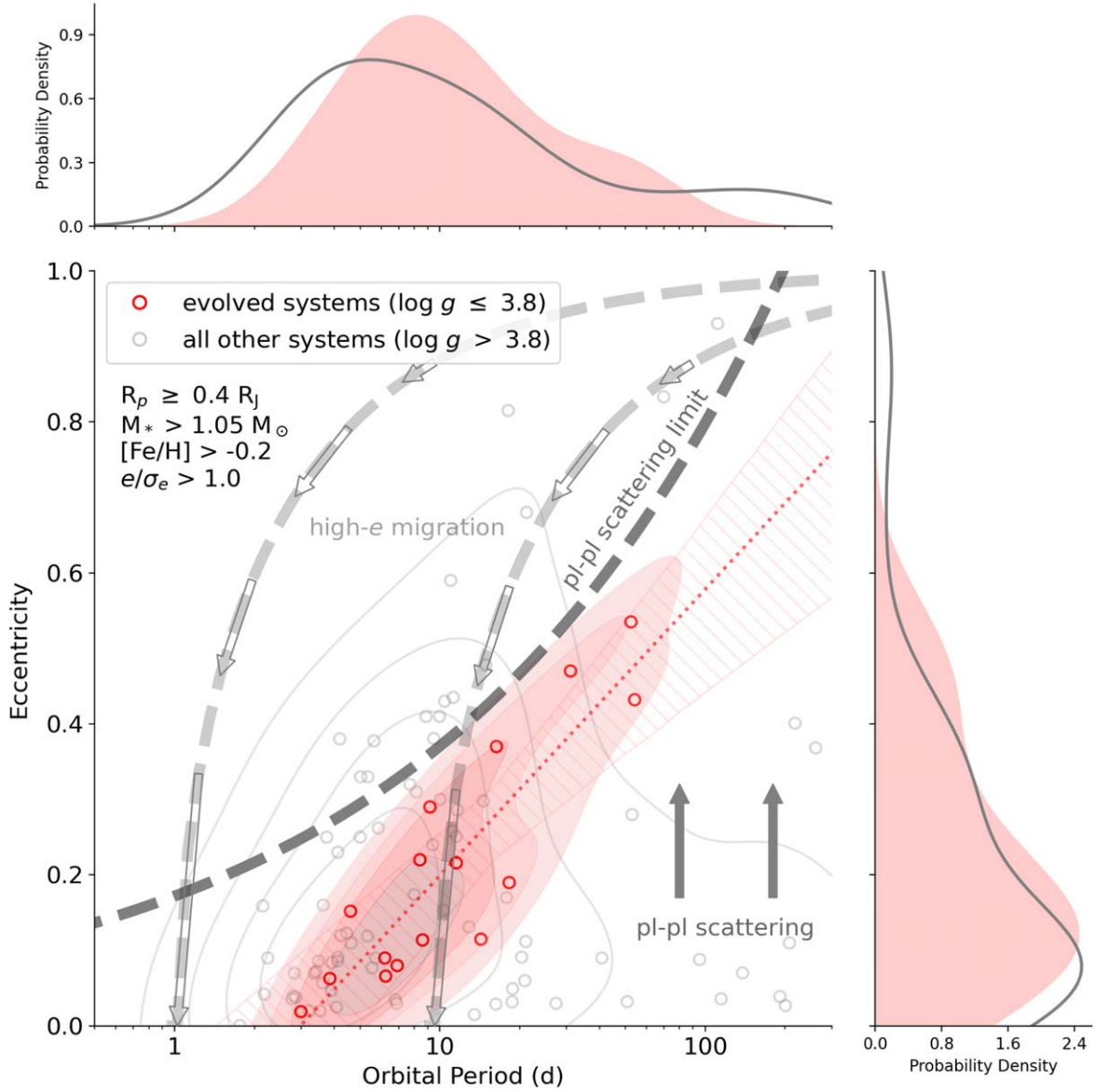


Figure 6. Eccentricity as a function of orbital period for planets in systems where $R_p \geq 0.4 R_J$, orbiting stars where $M_* > 1.05 M_\odot$ with metallicities > -0.2 dex, with significant eccentricities. Systems transiting evolved ($\log g \leq 3.8$) stars have been shown by the red contours and corresponding red points, while planets transiting main-sequence ($\log g > 3.8$) stars are shown by the gray contours and points. Tracks of constant orbital angular momentum followed during high-eccentricity migration are shown by the light-gray dotted lines and arrows, while the effects of planet–planet scattering and its approximate limit determined following the formulation noted in Dawson & Johnson (2018) are shown by the dark-gray arrows and dotted line. We find that planets transiting evolved stars appear to form a more linear distribution in period–eccentricity space than the rest of the planet population, possibly sculpted by these migration and scattering processes. Furthermore, we find that the orbital eccentricity of evolved systems can be approximated well by a linear regression to the logarithm of the orbital period, shown by the red dotted line and hatched region corresponding to a 95% confidence interval. A similar linear correlation is significantly weaker for the overall planet population.

system into angular momentum deficit, where the limiting scattering eccentricity $e_{\text{scatter,lim}}$ is defined here following the prescription of Dawson & Johnson (2018) as

$$e_{\text{scatter,lim}} \approx 0.2 \left(\frac{M_p}{0.5 M_J} \right)^{1/2} \left(\frac{2 R_J}{R_p} \right)^{1/2} \left(\frac{P}{3 \text{ days}} \right)^{1/3}, \quad (1)$$

assuming a typical planet mass of $0.5 M_J$ and planet radius of $1.3 R_J$. We show an approximate range for high-eccentricity migration following the formulation of Dawson & Johnson (2018), where

$$a_f = a(1 - e^2), \quad (2)$$

where e is the initial planet eccentricity and a_f is the final orbital separation, where we have assumed values of a_f between 0.03 and 0.09 au, as high-eccentricity migration would take less than 1 Myr for a typical gas giant planet to reach 0.03 au, yet it would take roughly 10 Gyr for the same planet to reach 0.09 au (Dawson & Johnson 2018).

To determine whether these two populations are distinct, we perform a two-dimensional Kolmogorov–Smirnov (K-S) test (Peacock 1983; Fasano & Franceschini 1987; Press et al. 2007) between these populations of planets transiting main-sequence and evolved stars. We find that the distribution of the population of evolved stars in the semimajor axis–eccentricity plane differs from the population of comparable main-sequence ($\log g > 3.8$) planets with a p -value of < 0.02 , implying that the

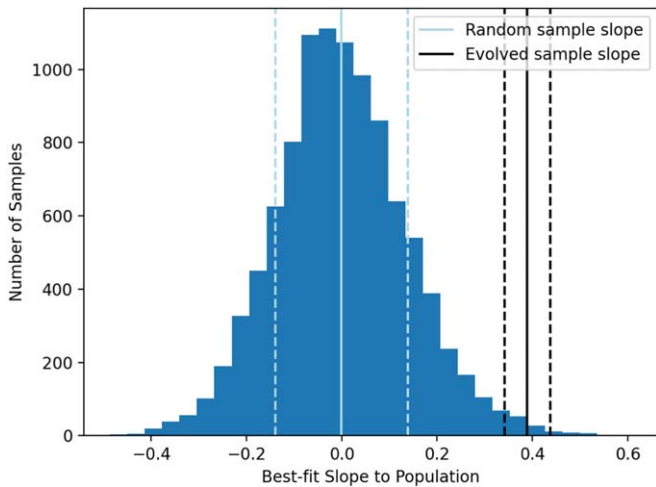


Figure 7. A comparison between the slope determined via a linear regression to the periods and eccentricities of evolved planets shown in Figure 6 (black) and a sample where random eccentricities are assigned to the evolved planets (blue), for all transiting planets with significant eccentricities. The number of samples in each bin is shown on the y-axis. The actual measured linear relation differs from the randomly determined population at a $>2\sigma$ level.

populations are significantly distinct. However, we also note that the significance of this result relies on the inclusion of the three systems with the highest orbital periods and eccentricities. The results of this analysis are thus subject to biases of small number statistics. We also compare the populations of masses and metallicities of the main-sequence and evolved host stars studied here, and we find that both comparisons have a p -value > 0.20 , implying that the masses and metallicities of the stellar host populations are not drawn from significantly different distributions.

In addition, we fit a linear regression to the period–eccentricity relation of the planet population orbiting evolved stars. We determine that the eccentricity of a planet in the evolved population $e \propto 0.38 \times \log_{10}(P/\text{days}) - 0.18$ for orbital periods between 3 and 1000 days. We find a Pearson correlation coefficient $r = 0.88$ for this population and a standard deviation from the estimated slope of 0.05. We also determine a similar fit to the larger planet population, and we find a relation where $e \propto 0.12 \times \log_{10}(P/\text{days})$, with a Pearson correlation coefficient $r = 0.35$, and a standard deviation from the estimated slope of 0.033, indicating that the period–eccentricity trends seen for single-planet transiting evolved systems differs from that of all similar mass and metallicity systems at $>5\sigma$ significance.

To test whether the observed features of this population are due to random chance, we produce a random permutation of the set of observed giant planet eccentricities and test how often the slope we recover for the observed evolved population is found in this reshuffled evolved population. We find that after 10,000 random resortings of eccentricities we recover a best-fit slope of 0.0 ± 0.15 , implying that our recovered eccentricity relation for evolved stars disagrees with a random population at a $>2\sigma$ level. We illustrate the results of our 10,000 fits to random draws in eccentricity in Figure 7.

Furthermore, we consider whether the observed trend for evolved systems could be due to detection biases. Planet detection via the transit method around evolved stars is biased toward detecting planets that transit more often and have larger transit depths. In addition, as specified in

Saunders et al. (2022), we smooth our light curves that are searched for transits with a median filter with a width of 2 days, which prevents the detection of transits that are longer than 48 hr. These effects will bias us toward finding shorter-period and larger planets around smaller stars, and thus the nondetection of short-period, eccentric planets around evolved stars cannot be due to a detection bias. As the length of a transit of a planet on an eccentric orbit depends on the argument of periastron ω (i.e., whether the transit occurs while the planet is at periastron, apastron, or in between) and transit duration $T_0 = T_{\text{circ}} \times \sqrt{1 - e^2} / (1 + e \cos \omega)$, where T_{circ} is the transit duration of a planet on an equivalent circular orbit, the change in transit duration for any value of $e \lesssim 0.5$ is less than a factor of 2. Furthermore, eccentric orbits result in a high transit probability with a “boost factor” proportional to $1/(1 - e^2)$, boosting transit probabilities by a factor of 1.33 or less for an eccentricity of 0.5 or less (Barnes 2007; Beatty & Seager 2010). These relatively small variations in transit probability and duration at all eccentricities observed in our sample imply that transit detection is largely independent of eccentricity if $e < 0.5$ at a given orbital period, and thus our nondetection of planets on circular orbits at periods beyond 10 days, where we do detect eccentric planets, is also not due to detection bias.

In Figure 8, we illustrate orbital eccentricity as a function of semimajor axis divided by stellar radius, again highlighting the evolved planet population. We find that the evolved planet population is largely indistinguishable from the larger planet population in this plane, where the only difference in the statistical distribution can be seen at the largest a/R_* values, which corresponds to periods that are too large to be detectable around many evolved stars. This indicates that the difference in planet orbital period and eccentricity distribution is likely sculpted by processes tied to a/R_* values, such as high-eccentricity migration and tidal interaction. This explains why the shortest-period planets around evolved stars are at longer orbits than the shortest-period planets around main-sequence stars (if a/R_* governs the inner boundary for allowed planet orbits, larger stars have a larger minimal separation), but it cannot explain the high eccentricities of evolved systems at longer periods. We find that if we compare the population of planets with a/R_* values > 8 , the mass and metallicity distributions overlap with two sample K-S test p -values > 0.5 , while the two-dimensional K-S test indicates that in e - a/R_* space, the probability of these systems coming from the same distribution is ≈ 0.03 . Furthermore, we illustrate stellar radius against planet eccentricity in the right panel of this figure. We see no clear correlation between eccentricity and stellar radius alone, again indicating that stellar radius alone is not driving the observed trend between period and eccentricity for this population, but rather that the trend at short periods is driven by tidal interactions governed by the a/R_* relation.

In general, these trends seen with stellar radius and age follow predicted planet orbital evolution theory: planet circularization and inspiral at small a/R_* are most strongly affected by stellar evolution due to exchange of angular momentum between the planet and the star (Villaver et al. 2014), while planet–planet scattering events are driven by secular chaos and thus become more likely over time (Veras et al. 2013). However, planet–planet scattering can also be impacted by the mass and composition of the host star and planets involved—planets formed around more massive and metal-rich stars tend to have higher eccentricities (Frelikh et al. 2019). We investigate

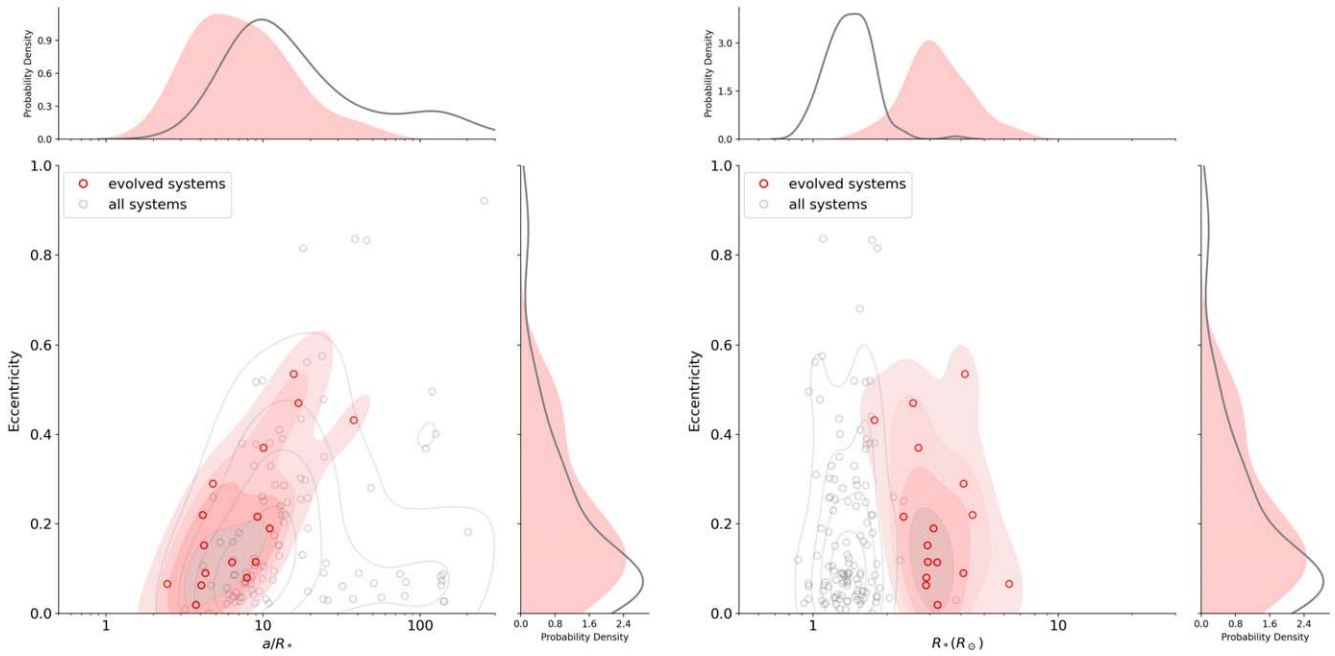


Figure 8. Left: orbital eccentricity as a function of semimajor axis divided by stellar radius, highlighting the evolved planet population in red. The evolved population seems to occupy similar ranges in eccentricity and a/R_* to the larger total planet population. Statistical tests suggest that differences between planet populations are insignificant in this plane. Right: orbital eccentricity as a function of stellar radius for the evolved (red) and overall (gray) planet populations. No clear correlation between stellar radius and eccentricity can be seen.

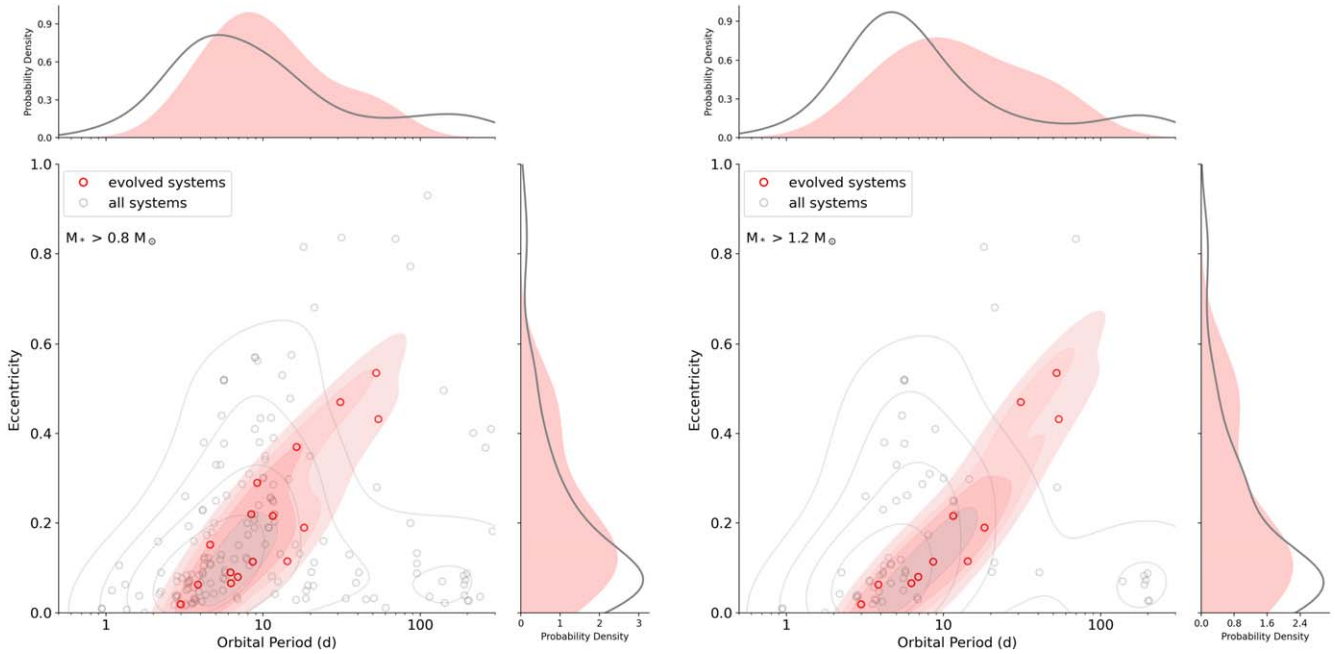


Figure 9. Same as Figure 6, except the cut on stellar mass has been changed, as stellar mass is known to be correlated with planet properties. We use a lower bound of $0.8 M_\odot$ on the left and $1.2 M_\odot$ on the right. The difference in planetary architectures between evolved and main-sequence systems appears robust with respect to stellar mass.

this in more depth in Figure 9, where we adjust our stellar mass cuts to $0.8 M_\odot$ (left) and $1.2 M_\odot$ (right).

We find that the populations of evolved and nonevolved massive stars overlap in e - a/R_* space and cannot be statistically distinguished. This suggests that stellar mass differences may also contribute to the observed period–eccentricity trend for evolved systems seen here, but it does not explain the relatively high eccentricities of planets orbiting somewhat lower mass (1.0 – $1.2 M_\odot$) evolved stars in our

sample. We repeat similar tests with metallicity cuts, replacing our previous cut with metallicity values of 0.0 and 0.2. Qualitatively, these cuts result in even tighter linear regressions (with Pearson r -values >0.95), but given the small samples of evolved stars considered ($\lesssim 5$), the statistical significance of this population difference is low. Thus, we do not show these relations in this paper, but we encourage future studies of this relation once more metal-rich evolved stars hosting transiting planets have been confirmed.

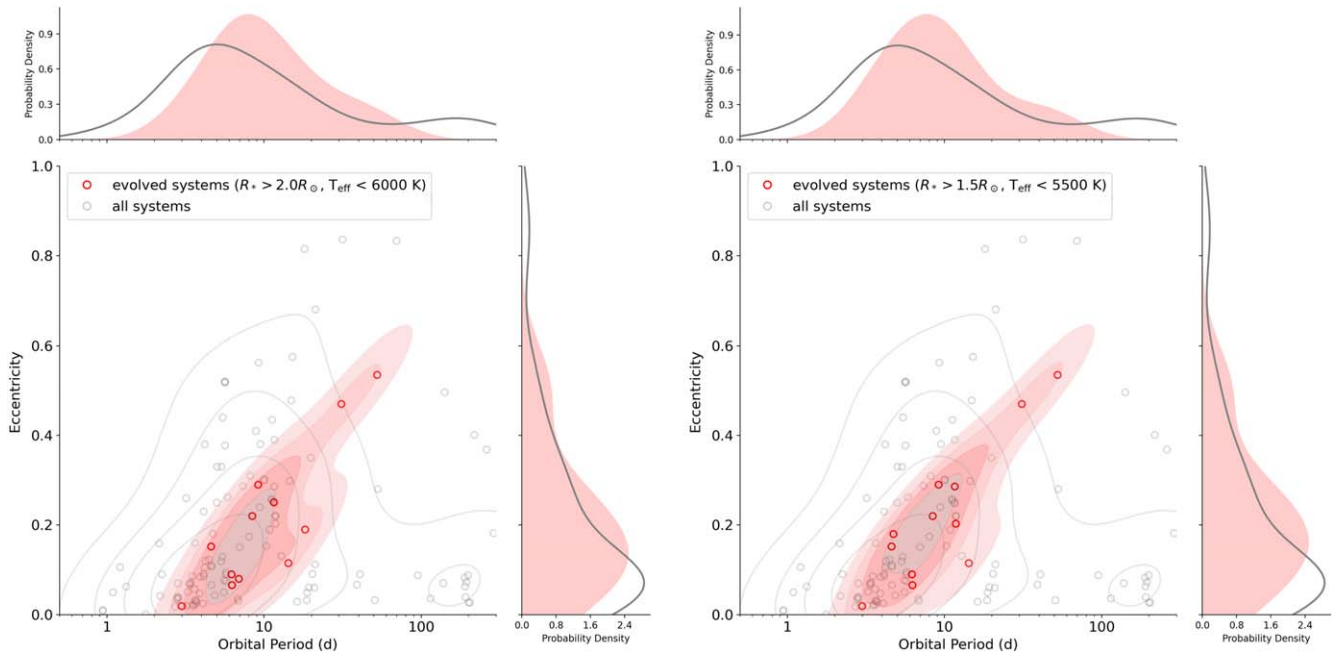


Figure 10. Same as Figure 6, except the population of evolved planets has been altered to instead include systems with host stars with radii $> 2.0 R_\odot$ and effective temperatures $T_{\text{eff}} < 6000$ K (left), or systems with host stars with radii $> 1.5 R_\odot$ and effective temperatures $T_{\text{eff}} < 5500$ K (right). The period–eccentricity relation seen in evolved systems appears comparably well constrained using these alternative definitions.

We then redefine the population of “evolved” systems by stellar effective temperature and radius in Figure 10. We define stars as evolved if $R_* > 2.0 R_\odot$ and $T_{\text{eff}} < 6000$ K on the left, and $R_* > 1.5 R_\odot$ and $T_{\text{eff}} < 5500$ K on the right. The redefinition of evolved to $R_* > 1.5 R_\odot$ and $T_{\text{eff}} < 5500$ K results in the inclusion of HD 89345 b, K2-108 b, and K2-261 b along with a subset of stars from Table 4 (Petigura et al. 2018; Van Eylen et al. 2018; Ikwut-Ukwa et al. 2020), whereas defining evolved as $R_* > 2.0 R_\odot$ and $T_{\text{eff}} < 6000$ K only results in the exclusion of some stars in Table 4. We find that, overall, both of these definitions of evolved stars appear to match well with our earlier definition of evolved stars, where the contour morphology is very similar, implying that our selection of evolved stars, as well as this observed dichotomy between the main-sequence and evolved star population, is robust.

We also note that we have restricted our comparisons to planets with radii larger than $0.4 R_J$ to avoid the issues of low completeness for transit detection of small planets orbiting evolved stars. However, the period–eccentricity distribution of smaller planets orbiting evolved stars may provide additional evidence confirming or refuting the trends seen here. In particular, Jofré et al. (2020) measured the eccentricities of two small planets in the evolved system Kepler-276 and found that both orbits were highly eccentric, with eccentricities > 0.6 . However, these planets were also found to be interacting with one another via transit timing variations, which suggests that their eccentricities may be governed by planet–planet interactions, as opposed to planet–star interaction. In contrast, the planets of the evolved system Kepler-56 appear to have eccentricities that are significantly lower than other planets orbiting evolved stars at similar orbital periods (Huber et al. 2013; Otor et al. 2016).

Furthermore, planets that have been confirmed orbiting evolved stars using only the RV method are suggested to feature low-eccentricity orbits, even at periods > 10 days (e.g., Takarada et al. 2018; Wolthoff et al. 2022). However, these

planets tend to be more massive, to be at wider orbital separations, and to orbit more evolved stars than the transiting planet sample. In addition, the detection biases for RV planet detection and orbital eccentricity characterization are much more difficult to disentangle than for transiting planets owing to the uneven time sampling of RV observations, and thus comparing the two planet populations in the period–eccentricity plane is not straightforward. The actual existence of up to 50% of the RV-only-detected planets orbiting evolved stars has recently been questioned owing to similar periods seen in magnetic activity indicators within the stellar spectra (Delgado Mena et al. 2018). Thus, we exclude planets without a transit measurement from our period–eccentricity analysis performed here and highlight the importance of a search for transiting planets on longer periods around evolved stars to properly characterize the orbital evolution of planets with separations beyond 0.5 au.

Theory has suggested that around an orbital distance of ~ 1 au an unstable equilibrium point is reached for the motion of planets with respect to stellar evolution, where planets within 1 au migrate inward and must eventually be engulfed by their host star, while planets beyond 1 au migrate outward owing to stellar mass loss and can survive stellar evolution through the helium flash, as their orbits are always beyond the stellar surface and tidal forces never become particularly strong for this population (Zahn 1977; Villaver et al. 2014). A search for planets on these periods around evolved stars can reveal whether stellar evolution creates a dearth of planets at these orbits, or whether planets on these orbits are perhaps more stable, or stable for a longer period of time than theories predict.

6. Orbital Decay of the Evolved Planet Population

The expected tidal interaction between hot gas giant planets and evolved host stars is expected to result in rapid orbital decay and eventual engulfment of the planet.

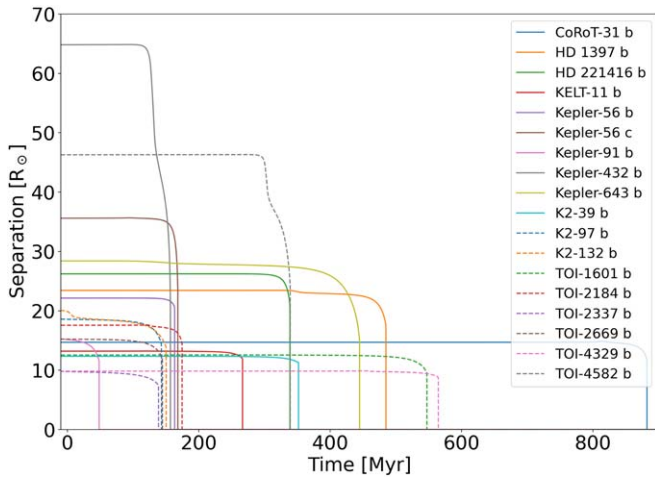


Figure 11. Expected orbital evolution of all evolved planetary systems considered in this study. Time into the future is shown on the x -axis, while orbital separation is shown on the y -axis. These systems show a wide range of orbital decay timescales spanning over an order of magnitude, but they do not appear to be decaying in a clear sequence according to period. This implies that the period–eccentricity relation identified is not an active evolutionary path for planetary systems undergoing circularization and inspiral, as there is no clear correlation between orbital period and inspiral timescale.

However, orbital decay has only been directly measured in one planetary system to date, which is significantly less evolved than the systems studied here (Yee et al. 2020; Turner et al. 2021; Wong et al. 2022). By constraining the rate of orbital decay in these systems, we can measure the strength of star–planet tidal interactions and their dependence on star and planet properties.

Figure 11 illustrates the expected orbital evolution of the evolved systems studied here over time as a function of orbital separation, calculated using the COSMIC binary evolution code package (Breivik et al. 2020), a binary population synthesis package based on the binary star evolution code base (Hurley et al. 2000, 2002). COSMIC includes the effects of the equilibrium tide with convective damping based on the standard approximations from Zahn (1977) and Zahn (1989) following the formalism of Hut (1981) and thus does not provide direct constraints on the static tidal quality factor Q'_* of the host stars, but it does account for the evolution of stellar structure over time, which governs the timescale of orbital decay. We find that all of these systems are expected to experience runaway inspiral in less than 1 Gyr, but the range in inspiral timescales for this population is quite large. Based on the results of COSMIC simulations for this sample of systems, planets on longer-period orbits do not seem to survive longer than planets on shorter-period orbits, indicating that the longer-period systems are not an earlier stage of the shorter-period systems in our sample, and the period–eccentricity relation identified here is not an evolutionary sequence or pathway for these systems. We also note that the evolutionary timescales listed here are longer than what has been predicted by other binary evolution studies (e.g., Sun et al. 2018), which is likely due to the treatment of dynamical tides and wave propagation within a star as it evolves along the subgiant and giant branches of evolution. Stellar winds and outflows and their associated drag forces may also play a role in inspiral at the latest stages (MacLeod et al. 2018).

7. Conclusions

In this paper, we have reported the discovery and characterization of TOI-4582 b, the latest planet discovered in our search for planets transiting evolved stars using TESS FFI data. Our main conclusions based on this discovery are listed as follows:

1. TOI-4582 b has one of the longest-period and most eccentric orbits found for a planet transiting an evolved star ($\log g < 3.8$).
2. The planet population transiting evolved stars appears to follow a loglinear trend in the period–eccentricity plane. This location may be explained by star–planet interaction causing tidal circularization and inspiral at small periods and planet–planet scattering events exciting orbital eccentricities at long periods.
3. Considering systems around evolved stars with one transiting planet, we find that these systems appear to follow a period–eccentricity correlation, where $e \approx 0.44 \log_{10}(P(\text{days})) - 0.25$ with a Pearson r correlation value > 0.85 and a standard deviation of 0.06. This is inconsistent with a similar linear fit to the population of all comparable planets at $> 5\sigma$ significance. A random draw of planetary eccentricities using a similar number of planets to that included in the evolved population studied here suggests that this trend is inconsistent with the null hypothesis at a $> 2\sigma$ significance. Additional tests using only higher-mass stars and slightly different definitions for an “evolved” stellar host suggest that these trends are robust.

The TOI-4582 b system highlights the importance of characterizing the longer-period transiting planet population of evolved stars to understand planetary system stability, as well as the need for a focused search to find systems with such long-duration transits. The extended TESS missions will extend continuous observations of hundreds of thousands of similar targets to 50 days or more of coverage. Furthermore, the higher-cadence and longer-baseline extended mission observations of TOI-4582 b may allow asteroseismic characterization of this and similar systems (Grunblatt et al. 2022). Similar continuous coverage of evolved stars with next-generation surveys such as PLATO will allow for the detection of smaller, less massive planets transiting evolved stars at longer periods (Rauer et al. 2014; Veras et al. 2015). Constraining the orbital properties of these longer-period, smaller planets will be essential for predicting the stability of rocky planets like our own around evolving stars, as well as around more massive stars. Observation of these stars will also be possible at greater distances because of their intrinsic brightnesses (Malmquist 1922), allowing comparison of planet demographics between Galactic thin- and thick-disk stars, as well as in other Galactic regions, where stellar populations are known to have different intrinsic properties.

We acknowledge the members of the Astro Data Group at the Center for Computational Astrophysics and the Stellar Rotation group at the American Museum of Natural History for very helpful discussions. We acknowledge the use of public TESS data from pipelines at the TESS Science Office and at the TESS Science Processing Operations Center. Resources supporting this work were provided by the NASA High-End Computing (HEC) Program through the NASA Advanced

Supercomputing (NAS) Division at Ames Research Center for the production of the SPOC data products. This work was supported by a NASA Keck PI Data Award, administered by the NASA Exoplanet Science Institute. Data presented herein were obtained at the W. M. Keck Observatory from telescope time allocated to the National Aeronautics and Space Administration through the agency's scientific partnership with the California Institute of Technology and the University of California. The Observatory was made possible by the generous financial support of the W. M. Keck Foundation. The authors wish to recognize and acknowledge the very significant cultural role and reverence that the summit of Maunakea has always had within the indigenous Hawaiian community. We are most fortunate to have the opportunity to conduct observations from this mountain. S.G., N.S., and D.H. acknowledge support by the National Aeronautics and Space Administration under grants 80NSSC19K0593 and 80NSSC21K0781 issued through the TESS Guest Investigator Program. D.H. acknowledges support from the Alfred P. Sloan Foundation and the National Aeronautics and Space Administration (80NSSC21K0652) and the National Science Foundation (80NSSC21K0652). N.S. acknowledges support from the National Science Foundation through the Graduate Research Fellowship Program under grants 1842402 and DGE-1752134. D.V. gratefully acknowledges the support of the STFC via an Ernest Rutherford Fellowship (grant ST/P003850/1). B.S.S. and I.A.S. acknowledge the support of the Ministry of Science and Higher Education of the Russian Federation under grant 075-15-2020-780 (N13.1902.21.0039). D. D. acknowledges support from the TESS Guest Investigator Program grants 80NSSC21K0108 and 80NSSC22K0185. Any opinions, findings, and conclusions or recommendations expressed in this material are those of the authors and do not necessarily reflect the views of the National Science Foundation. This research has made use of the Exoplanet Follow-up Observation Program website, which is operated by the California Institute of Technology, under contract with the National Aeronautics and Space Administration under the Exoplanet Exploration Program. Funding for the TESS mission is provided by NASA's Science Mission Directorate.

Software: This work relied heavily on open-source software tools, and we would like to thank the developers for their contributions to the astronomy community. For data access and detrending, this research made use of `lightkurve`, a Python package for Kepler and TESS data analysis (Lightkurve Collaboration et al. 2018); `TESSCut`, a MAST tool for extracting observations from TESS FFI (Brasseur et al. 2019); and `giants`, a pipeline for producing and detrending TESS FFI light curves (Saunders et al. 2022). The analysis portion of this research relied on `astropy` (Astropy Collaboration et al. 2013; Price-Whelan et al. 2018), as well as `exoplanet` (Foreman-Mackey et al. 2020) and its dependencies (Kipping 2013; Salvatier et al. 2016; Theano Development Team 2016; Agol et al. 2020; Luger et al. 2019; Foreman-Mackey et al. 2020).

ORCID iDs

Samuel K. Grunblatt  <https://orcid.org/0000-0003-4976-9980>
 Nicholas Saunders  <https://orcid.org/0000-0003-2657-3889>
 Ashley Chontos  <https://orcid.org/0000-0003-1125-2564>
 Soichiro Hattori  <https://orcid.org/0000-0002-0842-863X>
 Dimitri Veras  <https://orcid.org/0000-0001-8014-6162>

Daniel Huber  <https://orcid.org/0000-0001-8832-4488>
 Ruth Angus  <https://orcid.org/0000-0003-4540-5661>
 Malena Rice  <https://orcid.org/0000-0002-7670-670X>
 Katelyn Breivik  <https://orcid.org/0000-0001-5228-6598>
 Sarah Blunt  <https://orcid.org/0000-0002-3199-2888>
 Steven Giacalone  <https://orcid.org/0000-0002-8965-3969>
 Jack Lubin  <https://orcid.org/0000-0001-8342-7736>
 Howard Isaacson  <https://orcid.org/0000-0002-0531-1073>
 Andrew W. Howard  <https://orcid.org/0000-0001-8638-0320>
 David R. Ciardi  <https://orcid.org/0000-0002-5741-3047>
 Boris S. Safonov  <https://orcid.org/0000-0003-1713-3208>
 Ivan A. Strakhov  <https://orcid.org/0000-0003-0647-6133>
 David W. Latham  <https://orcid.org/0000-0001-9911-7388>
 Allyson Bieryla  <https://orcid.org/0000-0001-6637-5401>
 George R. Ricker  <https://orcid.org/0000-0003-2058-6662>
 Jon M. Jenkins  <https://orcid.org/0000-0002-4715-9460>
 Peter Tenenbaum  <https://orcid.org/0000-0002-1949-4720>
 Avi Shporer  <https://orcid.org/0000-0002-1836-3120>
 Edward H. Morgan  <https://orcid.org/0000-0003-1447-6344>
 Veselin Kostov  <https://orcid.org/0000-0001-9786-1031>
 Hugh P. Osborn  <https://orcid.org/0000-0002-4047-4724>
 Diana Dragomir  <https://orcid.org/0000-0003-2313-467X>
 Sara Seager  <https://orcid.org/0000-0002-6892-6948>
 Roland K. Vanderspek  <https://orcid.org/0000-0001-6763-6562>
 Joshua N. Winn  <https://orcid.org/0000-0002-4265-047X>

References

- Agol, E., Luger, R., & Foreman-Mackey, D. 2020, *AJ*, 159, 123
 Almenara, J. M., Damiani, C., Bouchy, F., et al. 2015, *A&A*, 575, A71
 Astropy Collaboration, Robitaille, T. P., Tollerud, E. J., et al. 2013, *A&A*, 558, A33
 Barclay, T., Endl, M., Huber, D., et al. 2015, *ApJ*, 800, 46
 Barclay, T., Pepper, J., & Quintana, E. V. 2018, *ApJS*, 239, 2
 Barnes, J. 2007, *PASP*, 119, 986
 Beatty, T. G., & Seager, S. 2010, *ApJ*, 712, 1433
 Bellm, E. C., Kulkarni, S. R., Graham, M. J., et al. 2019, *PASP*, 131, 018002
 Borucki, W. J., Koch, D., Basri, G., et al. 2010, *Sci*, 327, 977
 Brasseur, C. E., Phillip, C., Fleming, S. W., Mullally, S. E., & White, R. L. 2019, *Astrocute: Tools for creating cutouts of TESS images*, *Astrophysics Source Code Library*, ascl:1905.007
 Breivik, K., Coughlin, S., Zevin, M., et al. 2020, *ApJ*, 898, 71
 Brown, T. M., Baliber, N., Bianco, F. B., et al. 2013, *PASP*, 125, 1031
 Buchhave, L. A., Latham, D. W., Johansen, A., et al. 2012, *Natur*, 486, 375
 Chatterjee, S., Ford, E. B., Matsumura, S., & Rasio, F. A. 2008, *ApJ*, 686, 580
 Choi, J., Dotter, A., Conroy, C., et al. 2016, *ApJ*, 823, 102
 Chontos, A., Huber, D., Latham, D. W., et al. 2019, *AJ*, 157, 192
 Ciceri, S., Lillo-Box, J., Southworth, J., et al. 2015, *A&A*, 573, L5
 Dawson, R. I., & Johnson, J. A. 2018, *ARA&A*, 56, 175
 Dawson, R. I., & Murray-Clay, R. A. 2013, *ApJL*, 767, L24
 Delgado Mena, E., Lovis, C., Santos, N. C., et al. 2018, *A&A*, 619, A2
 Dotter, A. 2016, *ApJS*, 222, 8
 Eisner, N. L., Barragán, O., Aigrain, S., et al. 2020, *MNRAS*, 494, 750
 Fasano, G., & Franceschini, A. 1987, *MNRAS*, 225, 155
 Foreman-Mackey, D., Luger, R., Czekala, I., et al. 2020, *exoplanet-dev/exoplanet v0.3.2*, Zenodo, doi:10.5281/zenodo.1998447
 Frelikh, R., Jang, H., Murray-Clay, R. A., & Petrovich, C. 2019, *ApJL*, 884, L47
 Fűrész, G., Szentgyorgyi, A. H., & Meibom, S. 2008, in *Precision Spectroscopy in Astrophysics*, ed. N. C. Santos et al. (Berlin: Springer), 287
 Grunblatt, S. K., Huber, D., Gaidos, E., et al. 2017, *AJ*, 154, 254
 Grunblatt, S. K., Huber, D., Gaidos, E., et al. 2018, *ApJL*, 861, L5
 Grunblatt, S. K., Huber, D., Gaidos, E., et al. 2019, *AJ*, 158, 227
 Grunblatt, S. K., Huber, D., Gaidos, E. J., et al. 2016, *AJ*, 152, 185
 Grunblatt, S. K., Saunders, N., Sun, M., et al. 2022, *AJ*, 163, 120
 Guerrero, N. M., Seager, S., Huang, C. X., et al. 2021, *ApJS*, 254, 39
 Hamer, J. H., & Schlaufman, K. C. 2019, *AJ*, 158, 190
 Hattori, S., Foreman-Mackey, D., Hogg, D. W., et al. 2022, *AJ*, 163, 284

- Hatzes, A. P., Cochran, W. D., Endl, M., et al. 2003, *ApJ*, 599, 1383
- Howell, S. B., Sobek, C., Haas, M., et al. 2014, *PASP*, 126, 398
- Huang, C. X., Vanderburg, A., Pál, A., et al. 2020, *RNAAS*, 4, 206
- Huber, D., Carter, J. A., Barbieri, M., et al. 2013, *Sci*, 342, 331
- Huber, D., Chaplin, W. J., Chontos, A., et al. 2019, *AJ*, 157, 245
- Huber, D., Zinn, J., Bojesen-Hansen, M., et al. 2017, *ApJ*, 844, 102
- Hurley, J. R., Pols, O. R., & Tout, C. A. 2000, *MNRAS*, 315, 543
- Hurley, J. R., Tout, C. A., & Pols, O. R. 2002, *MNRAS*, 329, 897
- Hut, P. 1981, *A&A*, 99, 126
- Ikwut-Ukwa, M., Rodriguez, J. E., Bieryla, A., et al. 2020, *AJ*, 160, 209
- Jenkins, J. M. 2002, *ApJ*, 575, 493
- Jenkins, J. M., Caldwell, D. A., Chandrasekaran, H., et al. 2010, *ApJL*, 713, L87
- Jenkins, J. M., Tenenbaum, P., Seader, S., et al. 2020, Kepler Data Processing Handbook: Transiting Planet Search, Kepler Science Document, KSCI-19081-003
- Jenkins, J. M., Twicken, J. D., McCauliff, S., et al. 2016, *Proc. SPIE*, 9913, 99133E
- Jofré, E., Almenara, J. M., Petrucci, R., et al. 2020, *A&A*, 634, A29
- Jones, M. I., Brahm, R., Espinoza, N., et al. 2018, *A&A*, 613, A76
- Jones, M. I., Jenkins, J. S., Bluhm, P., Rojo, P., & Melo, C. H. F. 2014, *A&A*, 566, A113
- Khandelwal, A., Chaturvedi, P., Chakraborty, A., et al. 2022, *MNRAS*, 509, 3339
- Kipping, D. M. 2013, *MNRAS*, 435, 2152
- Kipping, D. M., Spiegel, D. S., & Sasselov, D. D. 2013, *MNRAS: Letters*, 434, L51
- Kolbl, R., Marcy, G. W., Isaacson, H., & Howard, A. W. 2015, *AJ*, 149, 18
- Kunimoto, M., Winn, J. N., Ricker, G. R., & Vanderspek, R. 2022, *AJ*, 163, 290
- Li, J., Tenenbaum, P., Twicken, J. D., et al. 2019, *PASP*, 131, 024506
- Lightkurve Collaboration, Cardoso, J. V. d., & Hedges, C. 2018, Lightkurve: Kepler and TESS time series analysis in Python, Astrophysics Source Code Library, ascl:1812.013
- Lillo-Box, J., Barrado, D., Moya, A., et al. 2014, *A&A*, 562, A109
- Lopez, E. D., & Fortney, J. J. 2016, *ApJ*, 818, 4
- Luger, R., Agol, E., Foreman-Mackey, D., et al. 2019, *AJ*, 157, 64
- MacLeod, M., Cantiello, M., & Soares-Furtado, M. 2018, *ApJL*, 853, L1
- Malmquist, K. G. 1922, *MeLuF*, 100, 1
- Montalto, M., Malavolta, L., Gregorio, J., et al. 2022, *MNRAS*, 509, 2908
- Naoz, S. 2016, *ARA&A*, 54, 441
- Nelson, B., & Davis, W. D. 1972, *ApJ*, 174, 617
- Nielsen, L. D., Bouchy, F., Turner, O., et al. 2019, *A&A*, 623, A100
- Otor, O. J., Montet, B. T., Johnson, J. A., et al. 2016, *AJ*, 152, 165
- Paxton, B., Bildsten, L., Dotter, A., et al. 2011, *ApJS*, 192, 3
- Peacock, J. A. 1983, *MNRAS*, 202, 615
- Petigura, E. A. 2015, PhD thesis, Univ. California, Berkeley
- Petigura, E. A., Marcy, G. W., Winn, J. N., et al. 2018, *AJ*, 155, 89
- Petrovich, C. 2015a, *ApJ*, 799, 27
- Petrovich, C. 2015b, *ApJ*, 805, 75
- Press, W. H., Teukolsky, S. A., Vetterling, W. T., & Flannery, B. P. 2007, Numerical Recipes 3rd Edition: The Art of Scientific Computing (Cambridge: Cambridge Univ. Press)
- Price-Whelan, A. M., Sipőcz, B. M., Günther, H. M., et al. 2018, *AJ*, 156, 123
- Quinn, S. N., White, T., Latham, D. W., et al. 2015, *ApJ*, 803, 49
- Rauer, H., Catala, C., Aerts, C., et al. 2014, *ExA*, 38, 249
- Reffert, S., Bergmann, C., Quirrenbach, A., Trifonov, T., & Kunstler, A. 2015, *A&A*, 574, A116
- Ricker, G. R., Winn, J. N., Vanderspek, R., et al. 2014, *JATIS*, 1, 1
- Rodriguez, J. E., Quinn, S. N., Zhou, G., et al. 2021, *AJ*, 161, 194
- Safonov, B. S., Lysenko, P. A., & Dodin, A. V. 2017, *AstL*, 43, 344
- Salvatier, J., Wiecki, T. V., & Fonnesbeck, C. 2016, *PeerJ Comp. Sci.*, 2, e55
- Santos, A. R. G., Breton, S. N., Mathur, S., & García, R. A. 2021, *ApJS*, 255, 17
- Saunders, N., Grunblatt, S. K., Huber, D., et al. 2022, *AJ*, 163, 53
- Schlaufman, K. C., & Winn, J. N. 2013, *ApJ*, 772, 143
- Scott, N. J., Howell, S. B., Horch, E. P., & Everett, M. E. 2018, *PASP*, 130, 054502
- Smith, A. M. S., Gandolfi, D., Barragán, O., et al. 2017, *MNRAS*, 464, 2708
- Stassun, K. G., Oelkers, R. J., Paegert, M., et al. 2019, *AJ*, 158, 138
- Sullivan, P. W., Winn, J. N., Berta-Thompson, Z. K., et al. 2015, *ApJ*, 809, 77
- Sun, M., Arras, P., Weinberg, N. N., Troup, N. W., & Majewski, S. R. 2018, *MNRAS*, 481, 4077
- Takarada, T., Sato, B., Omiya, M., et al. 2018, *PASJ*, 70, 59
- Tayar, J., Claytor, Z. R., Huber, D., & van Saders, J. 2022, *ApJ*, 927, 31
- Theano Development Team 2016, arXiv:1605.02688
- Turner, J. D., Ridden-Harper, A., & Jayawardhana, R. 2021, *AJ*, 161, 72
- Twicken, J. D., Catanzarite, J. H., Clarke, B. D., et al. 2018, *PASP*, 130, 064502
- Ulmer-Moll, S., Lendl, M., Gill, S., et al. 2022, *A&A*, 666, A46
- Van Eylen, V., Albrecht, S., Gandolfi, D., et al. 2016, *AJ*, 152, 143
- Van Eylen, V., Albrecht, S., Huang, X., et al. 2019, *AJ*, 157, 61
- Van Eylen, V., Dai, F., Mathur, S., et al. 2018, *MNRAS*, 478, 4866
- Veras, D., Brown, D. J. A., Mustill, A. J., & Pollacco, D. 2015, *MNRAS*, 453, 67
- Veras, D., Mustill, A. J., Bonsor, A., & Wyatt, M. C. 2013, *MNRAS*, 431, 1686
- Villaver, E., & Livio, M. 2009, *ApJL*, 705, L81
- Villaver, E., Livio, M., Mustill, A. J., & Siess, L. 2014, *ApJ*, 794, 3
- Vogt, S. S., Allen, S. L., Bigelow, B. C., et al. 1994, *Proc. SPIE*, 2198, 362
- Wang, S., Jones, M., Shporer, A., et al. 2019, *AJ*, 157, 51
- Wittenmyer, R. A., Clark, J. T., Trifonov, T., et al. 2022, *AJ*, 163, 82
- Wolthoff, V., Reffert, S., Quirrenbach, A., et al. 2022, *A&A*, 661, A63
- Wong, I., Shporer, A., Vissapragada, S., et al. 2022, *AJ*, 163, 175
- Xie, J.-W., Dong, S., Zhu, Z., et al. 2016, *PNAS*, 113, 11431
- Yee, S. W., Winn, J. N., Knutson, H. A., et al. 2020, *ApJL*, 888, L5
- Zahn, J. P. 1977, *A&A*, 57, 383
- Zahn, J. P. 1989, *A&A*, 220, 112